AGU PUBLICATIONS

JGR

Journal of Geophysical Research: Space Physics

RESEARCH ARTICLE
10.1002/2016JA022470

Special Section:
Big Storms of the Van Allen Probes Era

RAM-SCB simulations of electron transport and plasma wave scattering during the October 2012 "double-dip" storm

V. K. Jordanova[1], W. Tu[1,2], Y. Chen[1], S. K. Morley[1], A.-D. Panaitescu[1], G. D. Reeves[1], and C. A. Kletzing[3]

[1]Space Science and Applications, Los Alamos National Laboratory, Los Alamos, New Mexico, USA, [2]Department of Physics and Astronomy, West Virginia University, Morgantown, West Virginia, USA, [3]Department of Physics and Astronomy, University of Iowa, Iowa City, Iowa, USA

Key Points:
- First RAM-SCB simulations with 2-D (MLT- and L-dependent) event-specific chorus wave models inferred from LEO and RBSP data
- The measured low-energy trapped and precipitating electron fluxes are well reproduced by magnetospheric convection
- Local acceleration by chorus waves intensifies the electron fluxes at energies E greater than approximately 50 keV and overestimates observations

Correspondence to:
V. K. Jordanova,
vania@lanl.gov

Citation:
Jordanova, V. K., W. Tu, Y. Chen, S. K. Morley, A.-D. Panaitescu, G. D. Reeves, and C. A. Kletzing (2016), RAM-SCB simulations of electron transport and plasma wave scattering during the October 2012 "double-dip" storm, *J. Geophys. Res. Space Physics*, *121*, 8712–8727, doi:10.1002/2016JA022470.

Received 1 FEB 2016
Accepted 3 SEP 2016
Accepted article online 13 SEP 2016
Published online 28 SEP 2016

Abstract Mechanisms for electron injection, trapping, and loss in the near-Earth space environment are investigated during the October 2012 "double-dip" storm using our ring current-atmosphere interactions model with self-consistent magnetic field (RAM-SCB). Pitch angle and energy scattering are included for the first time in RAM-SCB using *L* and magnetic local time (MLT)-dependent event-specific chorus wave models inferred from NOAA Polar-orbiting Operational Environmental Satellites (POES) and Van Allen Probes Electric and Magnetic Field Instrument Suite and Integrated Science observations. The dynamics of the source (approximately tens of keV) and seed (approximately hundreds of keV) populations of the radiation belts simulated with RAM-SCB is compared with Van Allen Probes Magnetic Electron Ion Spectrometer observations in the morning sector and with measurements from NOAA 15 satellite in the predawn and afternoon MLT sectors. We find that although the low-energy ($E < 100$ keV) electron fluxes are in good agreement with observations, increasing significantly by magnetospheric convection during both *SYM-H* dips while decreasing during the intermediate recovery phase, the injection of high-energy electrons is underestimated by this mechanism throughout the storm. Local acceleration by chorus waves intensifies the electron fluxes at $E \geq 50$ keV considerably, and RAM-SCB simulations overestimate the observed trapped fluxes by more than an order of magnitude; the precipitating fluxes simulated with RAM-SCB are weaker, and their temporal and spatial evolutions agree well with POES/Medium Energy Proton and Electron Detectors data.

1. Introduction

Understanding the physical processes that control the dynamics of energetic electrons in the inner magnetosphere is important for the protection of satellite and ground-based technologies. Electron fluxes that intensify during storm time could damage satellites in two important ways: (1) lower energy (keV) electrons cause surface charging by nonuniformly depositing their charge in spacecraft surfaces and driving potential differences which can damage electronics [*Thomsen et al.*, 2013] and (2) higher-energy (above ~1 MeV) electrons can penetrate the surface and accumulate within internal dielectrics causing deep-dielectric charging, the subsequent breakdown of which can lead to component failures [e.g., *Wrenn et al.*, 2002]. Accurate modeling and, ultimately, predicting electron fluxes that could cause hazardous space weather events, however, is challenging since the near-Earth system is strongly coupled. Relativistic electron fluxes can change drastically during active conditions, and their response to solar wind driving is not simple. Although initial analysis of MeV electron fluxes at geosynchronous orbit [*Paulikas and Blake*, 1979] indicated that they are well correlated with solar wind velocity, later studies [*Reeves et al.*, 2011] found that only the lower flux limit depends linearly on the solar wind speed while highest-electron fluxes can occur for any solar wind speed. The statistical distribution of keV electron fluxes was found to be remarkably similar to the distribution of MeV fluxes and showed distinctly nonlinear correlations to solar wind driving. The Van Allen Probes mission (previously known as the Radiation Belt Storm Probes, RBSP) was thus launched in August 2012 to investigate the dynamics of near-Earth fluxes of relativistic electrons and to help the development of models for specification and prediction of their space weather effects [*Kessel et al.*, 2013].

There are several processes that lead to the enhancement of electron fluxes in the near-Earth space environment. A traditional heating mechanism for the radiation belt (MeV) electrons is the inward transport of electrons across the geomagnetic field by radial diffusion leading to significant energization [*Schulz and Lanzerotti*, 1974], but the timescales are typically too slow to account for the observed variations.

This process could be enhanced by ultralow frequency (ULF) waves [e.g., *Hudson et al.*, 2000; *Elkington et al.*, 2003] driven by Kelvin-Helmholtz instabilities or solar wind pressure fluctuations. ULF waves can efficiently accelerate electrons through a drift-resonant interaction, and a strong correlation between electron fluxes and ULF activity has been observed, with large increases in wave power preceding electron flux enhancement at geosynchronous orbit [*Rostoker et al.*, 1998]. Similarly, the ring current (keV) electron fluxes increase after injection from the plasma sheet during substorm-associated dipolarization events [e.g., *Baker et al.*, 1996; *Birn et al.*, 1997; *Fu et al.*, 2011b] and earthward transport and energization [e.g., *Jordanova and Miyoshi*, 2005; *Liu et al.*, 2005]. The injected ~10 keV electrons provide the energy source for the generation of whistler mode waves [e.g., *Jordanova*, 2012, and references therein] which transfer the energy back to the particles and accelerate them to higher energies. The tens of keV ring current electrons are thus often referred to as the "source" population of the radiation belts [e.g., *Li and Temerin*, 2001; *Jaynes et al.*, 2015]. Likewise, the hundreds of keV fluxes are considered a "seed" population for the radiation belts as they may be accelerated to MeV energies by linear [e.g., *Horne and Thorne*, 1998; *Summers et al.*, 1998] or nonlinear [e.g., *Omura et al.*, 2007] interactions with very low frequency (VLF) whistlers and by interactions with fast magnetosonic waves [e.g., *Horne et al.*, 2007].

On the other hand, the decrease of the magnetic field strength during the main phase of a storm due to the ring current buildup causes an outward motion of energetic electrons through conservation of the third adiabatic invariant and a decrease of relativistic electron fluxes, the "*Dst* effect", first demonstrated for flux variations near geosynchronous orbit by *Kim and Chan* [1997]. Additional processes contributing to the loss of energetic electrons are outward radial diffusion combined with magnetopause shadowing [e.g., *Shprits et al.*, 2006; *Morley et al.*, 2010] and precipitation into Earth's atmosphere via wave-particle interactions [e.g., *Walt and MacDonald*, 1962]. Scattering into the atmospheric loss cone may be significant and includes electron precipitation by plasmaspheric hiss [e.g., *Lyons et al.*, 1972; *Meredith et al.*, 2006], by scattering by VLF chorus [e.g., *O'Brien et al.*, 2004; *Bortnik and Thorne*, 2007], and by electromagnetic ion cyclotron (EMIC) waves [e.g., *Thorne and Kennel*, 1971; *Jordanova et al.*, 2008]. The electron losses balance the energization processes [e.g., *Fu et al.*, 2011a] and thus constrain the rebuilding of the ring current and the radiation belts.

Recent studies using high-quality particle and wave data from the Van Allen Probes mission provided improved understanding of many of the physical processes discussed above that drive relativistic electron dynamics in near-Earth space. For example, the importance of local acceleration by plasma waves was demonstrated by *Reeves et al.* [2013] and *Thorne et al.* [2013], while the importance of gradual acceleration by radial diffusion was shown by *Baker et al.* [2014]. Significant physical insight on the simultaneously acting and highly variable transport, acceleration, and loss mechanisms was also gained from model simulations and their comparison with observations. It was thus shown that the enhancement of MeV electrons is higher when a self-consistent electric field model is used [*Fok et al.*, 2014] and that parameterized pitch angle loss rates could account for the trapped electron fluxes observed at geosynchronous orbit as well as for the precipitating fluxes observed in the ionosphere [*Chen et al.*, 2015]. A very interesting "double-dip" large geomagnetic storm, which is also the subject of this study, occurred shortly after the RBSP launch in October 2012 [*Reeves et al.*, 2013]. Previous numerical modeling simulations in two dimensions (2-D) [*Thorne et al.*, 2013] and three dimensions (3-D) [*Tu et al.*, 2014] reproduced the acceleration of MeV electrons using event-specific wave models. We investigate the dynamics of lower energy (keV) electrons, the generation of whistler mode waves, and the effects from subsequent wave-particle interactions in the inner magnetosphere using a four-dimensional (4-D) physics-based model, the ring current-atmosphere interactions model with self-consistent magnetic field (RAM-SCB) [*Jordanova et al.*, 2012]. The ring current electron fluxes represent the source (approximately tens of keV) and seed (approximately hundreds of keV) populations for relativistic electrons and are crucial elements for radiation belt evolution. We present quantitative comparisons between our model predictions and Van Allen Probes and NOAA Polar-orbiting Operational Environmental Satellites (POES) observations available during the investigated storm period.

2. Observations During the October 2012 Double-Dip Storm

Interplanetary observations and geomagnetic indices during 7–10 October 2012 taken from the OMNIWeb 5 min database are shown in Figure 1. Sharp increases in solar wind density, speed, and dynamic pressure are observed around ~05 UT 8 October (hour 29), indicative of the arrival of an interplanetary shock

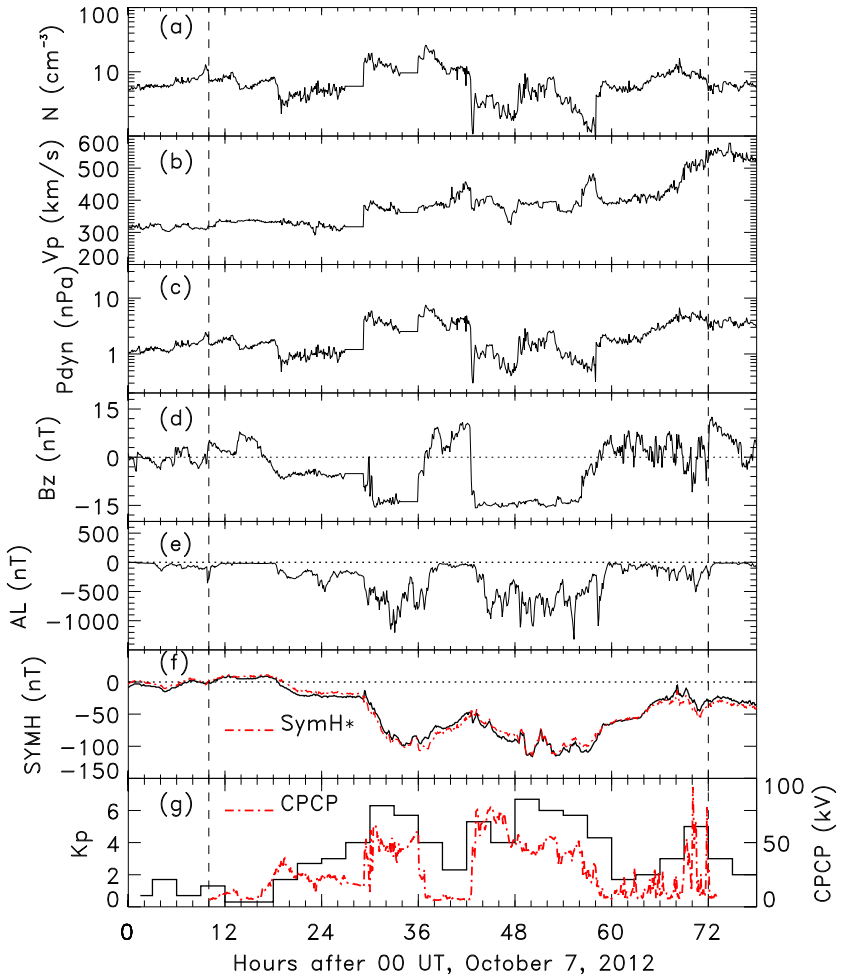

Figure 1. Interplanetary data and geomagnetic indices during 7–10 October 2012. (a) Proton density, (b) solar wind speed, (c) dynamic pressure, and (d) B_z (GSM) component of the magnetic field. (e) The *AL* index, (f) measured (solid) and pressure-corrected (dash-dotted) *SYM-H*, (g) the *Kp* index (solid) and the W05 cross polar cap potential drop (dash-dotted). The vertical dashed lines mark the time period of RAM-SCB simulation.

(Figures 1a–1c). The subsequent southward excursion of the interplanetary magnetic field (IMF) B_z component to about −15 nT (Figure 1d) triggered the first dip of a large geomagnetic storm with minimum *SYM-H* ≈ −100 nT at ~10 UT 8 October (hour 34) (Figure 1f). After an intermediate recovery to *SYM-H* ≈ −50 nT at ~18 UT (hour 42) during a short-lived northward IMF turning, the storm intensified again reaching a second dip of *SYM-H* ≈ −115 nT at ~02 UT 9 October (hour 50). The dynamic pressure was stronger during the first dip due to the larger solar wind density and compressed the magnetopause to <8 R_E; during the second dip the solar wind dynamic pressure decreased and the magnetopause moved out to >10 R_E [*Thorne et al.*, 2013]. The substorm activity intensified during both dips as shown by the *AL* index decreasing below −1000 nT (Figure 1e). The planetary *Kp* index reached maxima of 6^+ and 7^- at hour 30 and hour 48, while the cross polar cap potential (CPCP) drop obtained with the IMF-dependent *Weimer* [2005] (W05) ionospheric electric potential model peaked at approximately hour 30 and hour 42, respectively (Figure 1g). The solar wind speed fluctuated around 400 km/s until approximately hour 68 when it began a slow rise while the storm recovered to *SYM-H* ≈ 0.

Measurements during this period from the Magnetic Electron Ion Spectrometer (MagEIS) [*Blake et al.*, 2013] and Electric and Magnetic Field Instrument Suite and Integrated Science (EMFISIS) investigation [*Kletzing et al.*, 2013] on board the Van Allen Probe A, along an elliptical orbit on the morning side with apogee at ~6 R_E and MLT≈7, are displayed in Figure 2. The panels show, from top to bottom, the spin-averaged differential electron flux as a function of energy from ~30 to 350 keV, the electron flux magnitude at four representative energies, the whistler wave power spectral density, and the *L* shell [*McIlwain*, 1966] as a function of time (horizontal axis).

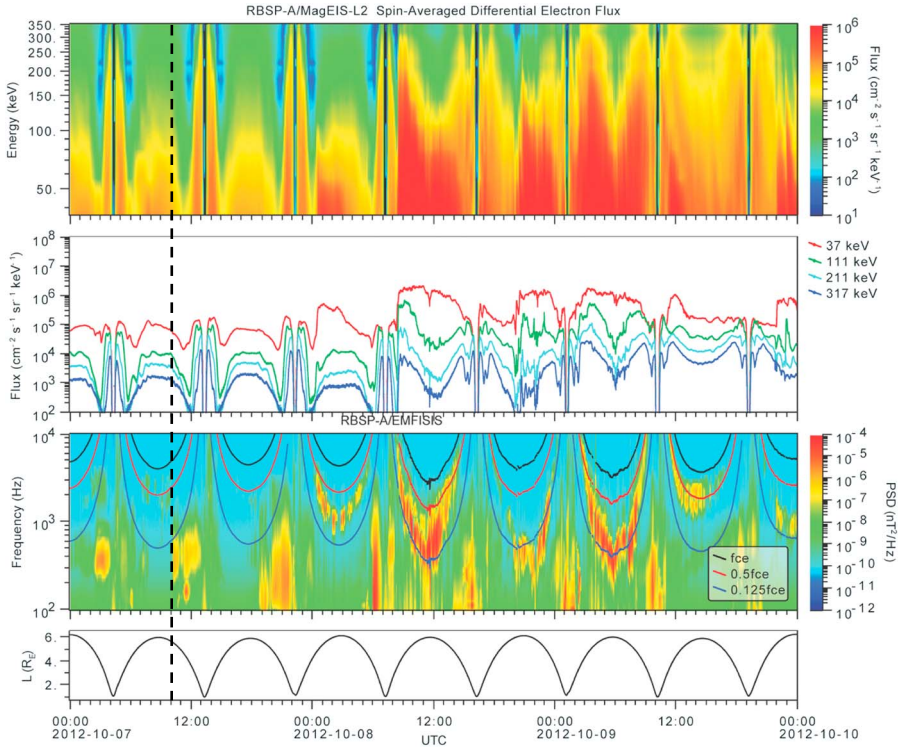

Figure 2. Van Allen Probe A observations during 7–9 October 2012 including (top to bottom) MagEIS differential electron flux spectrogram; spin-averaged electron flux at 37 keV (red), 111 keV (green), 211 keV (light blue), and 317 keV (dark blue); EMFISIS magnetic field power spectral density spectrogram with lines denoting fractions of the electron gyrofrequency at 0.1 f_{ce} (blue), 0.5 f_{ce} (red) and 1.0 f_{ce} (black); and the McIlwain L parameter along the satellite orbit. The vertical dashed line marks the start of RAM-SCB simulation.

As seen from the MagEIS flux data, during 7 October the satellite traversed several times at low $L < 4$ the electron ring current characterized by quiet time fluxes extending from ~30 to 350 keV; the ~40 keV flux was of the order of 10^5 cm^{-2} s^{-1} sr^{-1} keV^{-1}, and the flux decreased at larger energies. This trapped population was clearly separated from the <100 keV population on open drift paths at larger L shells. With the development of substorm activity, a dispersionless electron injection was observed at <100 keV energies at ~01 UT on 8 October that reached $L \approx 5$ at MLT ≈ 5. The next nightside satellite pass occurred during the storm main phase from ~07 to ~12 UT 8 October, and MagEIS measured enhanced electron fluxes typical of a strong ring current with fluxes at higher energies (>100 keV) confined to lower L shells. The electron fluxes decreased at all energies from ~14 UT to ~18 UT as the storm recovered. Several electron injections occurred after ~20 UT 8 October and throughout 9 October during the second *SYM-H* dip when the ring current intensified even more but the electron flux enhancement remained at $E \leq 150$ keV at apogee. EMFISIS observations of interest to this study showed weakly enhanced lower band chorus ($f < 0.5f_{ce}$) concurrent with the enhancement of ~30–50 keV electrons during the initial substorm activity on ~01–05 UT 8 October. The power spectral density increased significantly in this frequency band during the first and second *SYM-H* minima, while it was reduced during the intermediate storm recovery. On the other hand, low-frequency ($f < 0.1f_{ce}$) hiss was observed mostly at small radial distances on the dayside when the satellite passed briefly through the plasmasphere.

Figure 3 shows observations from one of the NOAA POES satellites which have circular Sun-synchronous orbits (altitude ~800–850 km with an inclination of ~98°) and a period of ~102 min. The Space Environment Monitor 2 (SEM2) [*Evans and Greer*, 2000] on board each three-axis stabilized POES spacecraft includes a set of solid-state Medium Energy Proton and Electron Detectors (MEPED). For electrons, there are two solid-state detector telescopes, one pointing toward zenith (i.e., the 0° telescope) and the other to view at about 90° to the first (i.e., the 90° telescope), to measure electrons in three energy ranges (E1 = 0.03–2.5 MeV, E2 = 0.1–2.5 MeV, and E3 = 0.3–2.5 MeV). In the outer belt region, the 0° telescope measures precipitating electrons inside the loss cone, while the 90° telescope measures electrons that are locally trapped [*Rodger et al.*, 2010]. The electrons' radial distributions measured by NOAA 15, which samples in the predawn and

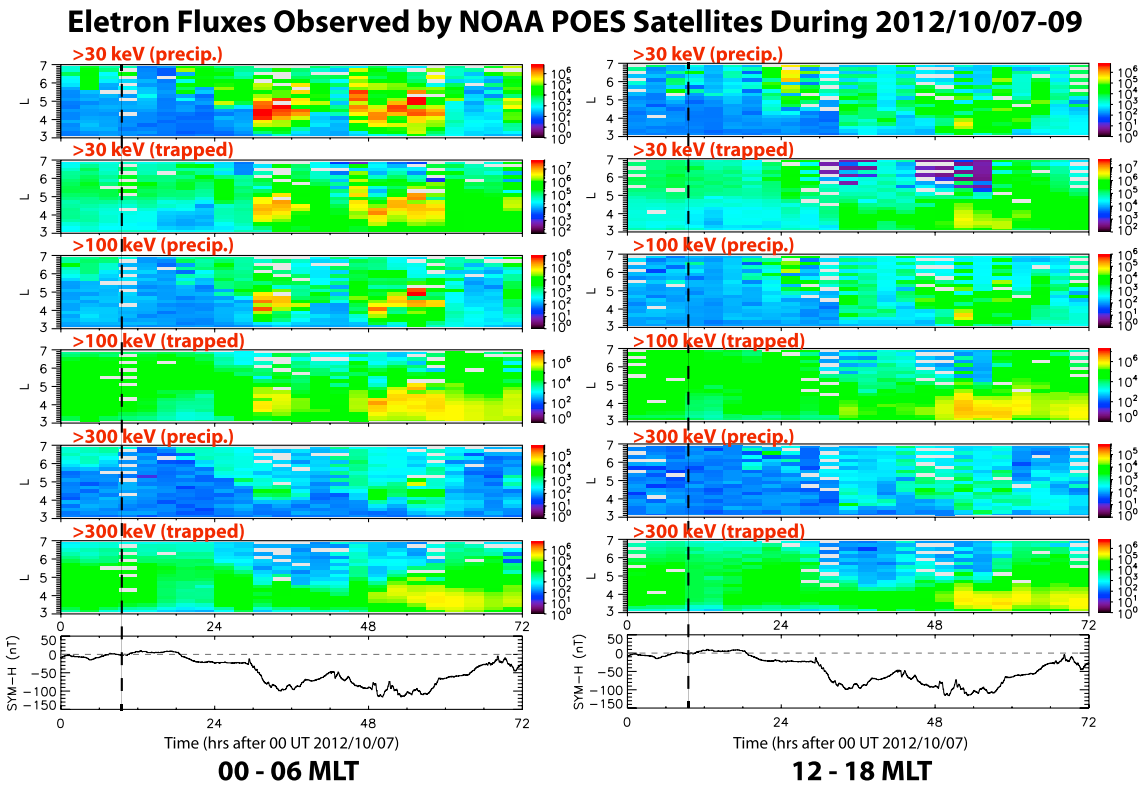

Figure 3. The NOAA POES precipitating and trapped electron fluxes (in units of 1/cm^2/s/sr) during 7–9 October 2012 binned into three energy ranges (>30 keV, >100 keV, and >300 keV), (left column) for MLT = 0–6 and (right) for MLT = 12–18 local time sectors. By comparing to MEPED proton data following the method used by *Chen et al.* [2012], we confirmed that protons have no significant contaminations on electron data during the period. The *SYM-H* index is given for reference, and the vertical lines mark the start of RAM-SCB simulation.

afternoon sectors, over a 3 day period, are presented in Figure 3. Here the electron fluxes are binned into 3 h intervals and sorted by precipitating versus trapped populations for three energy ranges (E1, E2, and E3) and two local time sectors. In comparison with the prestorm quiet time flux level, both the precipitating and trapped fluxes intensified at $3< L <6$ predawn in the lowest energy range (E1) during the first *SYM-H* dip. The increase was smaller in the afternoon sector and at higher energies. On the other hand, the fluxes increased at all energies and all local times during the second *SYM-H* dip and the intensification of the trapped fluxes at higher energies lasted throughout the recovery phase.

Electron and ion flux measurements from the MagEIS instruments on the Van Allen Probes A and B and from the Magnetospheric Plasma Analyzer (MPA) and Synchronous Orbit Particle Analyzer (SOPA) instruments on LANL-GEO satellites during 3 days of the October 2012 storm are plotted in Figure 4. For these comparisons, the LANL-GEO fluxes at 6.6 R_E are interpolated in time and MLT to the epoch and MLT of Van Allen Probes' apogee. It is evident that the fluxes from the different instruments agree reasonably well, especially at lower (<200 keV) energies of interest to this study, when interpolated to the nearly same epoch and location in the magnetosphere. The agreement is better during the prestorm period on 7 October than during the more disturbed time on 8 and 9 October when temporal flux variations are clearly seen. The LANL-GEO fluxes are used as boundary conditions for the stand-alone RAM-SCB simulations.

3. RAM-SCB Model Developments

We simulate the ring current evolution during the double-dip storm of 7–9 October 2012 using our RAM-SCB model which couples the ring current-atmosphere interactions model (RAM) [*Jordanova et al.*, 1997, 2010b] with the Euler-potential-based plasma equilibrium code [*Zaharia et al.*, 2006, 2010]. This model has been used successfully in many ring current studies over the past decade; therefore, only a brief description of RAM-SCB focusing on its recent development is given below. The 4-D RAM solves the kinetic equation for H^+, O^+, He^+, and electron phase space distributions $Q_l(R_o, \phi, E, \mu_o, t)$ in the magnetic equatorial plane as a function of time

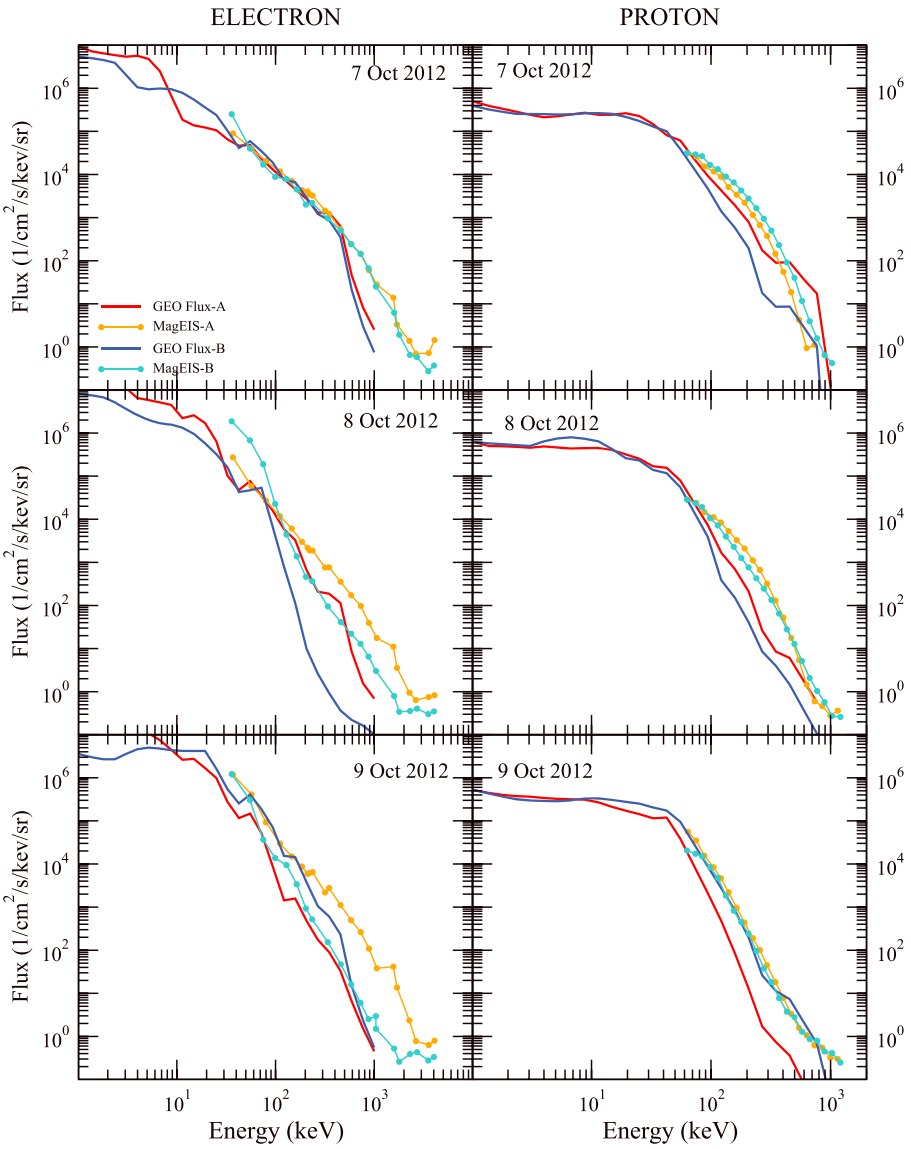

Figure 4. A comparison between (left column) electron and (right column) ion fluxes from the MagEIS instruments (dotted) on the Van Allen Probes A and B and from the MPA and SOPA instruments (solid) on LANL-GEO satellites during 7–9 October 2012. The LANL-GEO fluxes are interpolated in time and MLT to the epoch and MLT of Van Allen Probes' apogee. Only the first Van Allen Probe apogee of each day is used.

t, radial distance from Earth (R_o from 2 to 6.5 R_E), geomagnetic east longitude ϕ, kinetic energy E from ~100 eV to ~400 keV, and equatorial pitch angle α_o from 0° to 90°:

$$\frac{\partial Q_l}{\partial t}+\frac{1}{R_o^2}\frac{\partial}{\partial R_o}\left(R_o^2\langle\frac{dR_o}{dt}\rangle Q_l\right)+\frac{\partial}{\partial\phi}\left(\langle\frac{d\phi}{dt}\rangle Q_l\right)+\frac{1}{\gamma p}\frac{\partial}{\partial E}\left(\gamma p\langle\frac{dE}{dt}\rangle Q_l\right)$$
$$+\frac{1}{h\mu_o}\frac{\partial}{\partial\mu_o}\left(h\mu_o\langle\frac{d\mu_o}{dt}\rangle Q_l\right)=\langle\left(\frac{\partial Q_l}{\partial t}\right)_{\text{loss}}\rangle \quad (1)$$

Here the brackets $\langle\rangle$ denote bounce-averaging, $\mu_o = \cos(\alpha_o)$, p is the relativistic momentum of the particle, and γ is the relativistic factor. The integral $h = 1/(2R_o)\int ds/\sqrt{(1-B(s)/B_m)}$ is calculated along the magnetic field lines and between the mirror points where the field intensity is B_m.

The equatorial anisotropic plasma pressure produced by the ring current particles is mapped along the field lines and used by the 3-D Euler-potential-based equilibrium code to calculate the resulting force-balanced magnetic field [e.g., *Zaharia et al.*, 2006]. This self-consistent magnetic field is passed back to RAM in order to propagate the phase space distributions. In the stand-alone RAM-SCB the electric field is provided from the

latest version of the solar wind-driven W05 ionospheric model (Figure 1g) by mapping it along the SCB field lines to the equatorial plane and adding corotation; the process of radial diffusion is not considered. The nightside boundary conditions are determined from plasma sheet flux measurements from the MPA and SOPA instruments on the LANL geosynchronous spacecraft (Figure 4). In this study we assume isotropic plasma boundary conditions, although anisotropic electron pitch angle distributions like "cigar-type" or "pancake-type" have been observed in the plasma sheet behind dipolarization fronts [e.g., *Fu et al.*, 2011b, 2012]; their effect will be considered in future work. To set the initial conditions, we use quiet time measurements during October 2012 from the MagEIS and HOPE [*Funsten et al.*, 2013] instruments which are part of the Energetic particle, Composition, and Thermal plasma (ECT) suite [*Spence et al.*, 2013] on the Van Allen Probes, starting the simulation at 10 UT 7 October well before the storm commencement (Figure 1). The dayside boundary conditions correspond to free particle outflow. Additional loss processes included in this study are charge exchange of ring current ions with geocoronal hydrogen, and ion and electron precipitation due to collisions with the dense atmosphere assuming a loss cone boundary of 200 km altitude.

After injection from the plasma sheet, the electron population becomes unstable as the particles drift through the inner magnetosphere and undergo further acceleration and loss processes. To investigate the free energy available for the excitation of whistler mode waves during the 7–9 October 2012 storm period, we performed initial simulations of electron dynamics considering a simplified loss term (Q_e/τ_{wp}) where (τ_{wp}) is the wave-particle interactions lifetime. In this case electron losses inside the plasmasphere were included using lifetimes calculated after *Albert* [1999], while losses due to whistler mode wave scattering outside the plasmasphere were incorporated using empirical lifetimes for diffusion that is not strong everywhere (for further details, see *Jordanova et al.* [2008, 2010a, and references therein]). The linear growth rate of whistler mode chorus was calculated in the equatorial plane using the electron distributions and self-consistent magnetic field simulated with RAM-SCB and cold plasma density simulated with the coupled plasmasphere model [*Rasmussen et al.*, 1993, *Jordanova et al.*, 2010a]. These RAM-SCB simulation results are compared with the wave proxy derived from POES data at three representative times (prestorm, main, and recovery phase) in Figure 5 (left, middle, and right columns, respectively). The linear growth rate of parallel propagating chorus in the lower band frequency range (Figure 5a) intensifies significantly during the storm main phase. This is due to the increased effective electron anisotropy (Figure 5b, as defined in *Jordanova et al.* [2010a, equation (2)]) that develops at outer L shells when particles drift in realistic magnetic field and undergo large acceleration and drift shell splitting [*Jordanova et al.*, 2012]. In agreement with previous studies, the growth rate maximizes in the morning sector outside the plasmasphere, as indicated by the cold plasma density (Figure 5c); the corresponding parallel energy of resonant electrons is from ~2 to 5 keV. During the prestorm and recovery phases the electron fluxes are smaller and the anisotropy is not sufficient to excite significant whistler wave growth. Figure 5d shows 2-D snapshots of equatorial chorus wave amplitudes inferred from the precipitating 30 keV electron fluxes measured at low altitude by multiple NOAA POES satellites [*Chen et al.*, 2014]. Specifically, the measured precipitating electron fluxes are related with an adjustable parameter to the equatorial wave measurements made by EMFISIS onboard Van Allen Probes to infer the global distribution of chorus waves. A previous study by *Tu et al.* [2014] has shown that the obtained amplitudes are in good agreement with in situ EMFISIS observations during this storm (Figure 2); their spatial and temporal evolutions also agree reasonably well with the global patterns of chorus wave growth simulated with RAM-SCB (Figure 5a).

To implement in RAM-SCB for the first time quasi-linear diffusion of relativistic electrons by whistler mode waves, we include diffusion in pitch angle and energy as the most important terms (mixed diffusion will be considered in future extensions of this work) on the right-hand side of equation (1) following *Jordanova et al.* [1997, 1998]:

$$\left\langle \left(\frac{\partial Q_l}{\partial t} \right)_{wp} \right\rangle = \frac{1}{h\mu_o} \frac{\partial}{\partial \mu_o} \left[h\mu_o \langle D_{\mu_o\mu_o} \rangle \frac{\partial Q_l}{\partial \mu_o} \right] + \frac{1}{\gamma p} \frac{\partial}{\partial E} \left[\gamma p \langle D_{EE} \rangle \frac{\partial Q_l}{\partial E} \right] \tag{2}$$

Here the bounce-averaged quasi-linear pitch angle and energy diffusion coefficients are:

$$\langle D_{\mu_o\mu_o} \rangle = \frac{(1-{\mu_o}^2)}{2h{\mu_o}^2 R_o} \int_{s_m}^{s'_m} \mu \frac{B_o}{B} \frac{D_{\alpha_o\alpha_o}}{p^2} ds = \frac{(1-{\mu_o}^2)}{p^2} \langle D_{\alpha_o\alpha_o} \rangle \tag{3}$$

$$\langle D_{EE} \rangle = \frac{p^2}{2h\gamma^2 m_o^2 R_o} \int_{s_m}^{s'_m} \frac{D_{pp}}{\mu} ds = \frac{p^2}{m_o^2 \gamma^2} \langle D_{pp} \rangle \tag{4}$$

where m_o is the rest mass of the resonating particle and s_m denotes the mirror point.

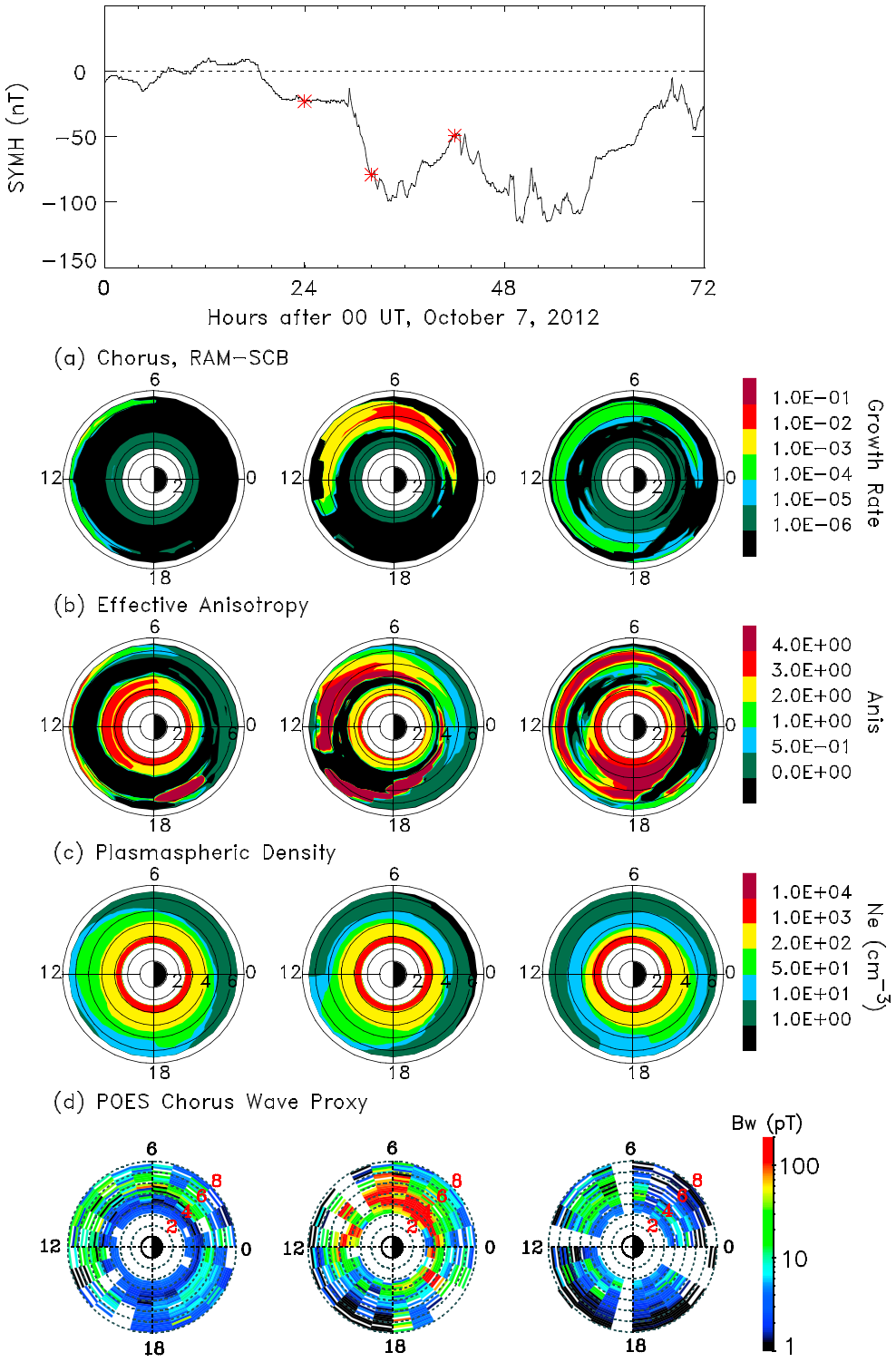

Figure 5. (a) Normalized growth rate of whistler mode chorus with frequency 0.45 f_{ce} calculated with RAM-SCB, (b) effective anisotropy of ring current electrons, and (c) cold plasma density. (d) Proxy for chorus wave amplitude (defined as the square root of wave intensity integrated over [0.1–0.8] f_{ce}); data gaps are due to the limited spatial coverage of POES satellites. All parameters are plotted in the equatorial plane at hours 24, 32, and 42 after 00 UT 7 October 2012 indicated with stars in the *SYM-H* plot.

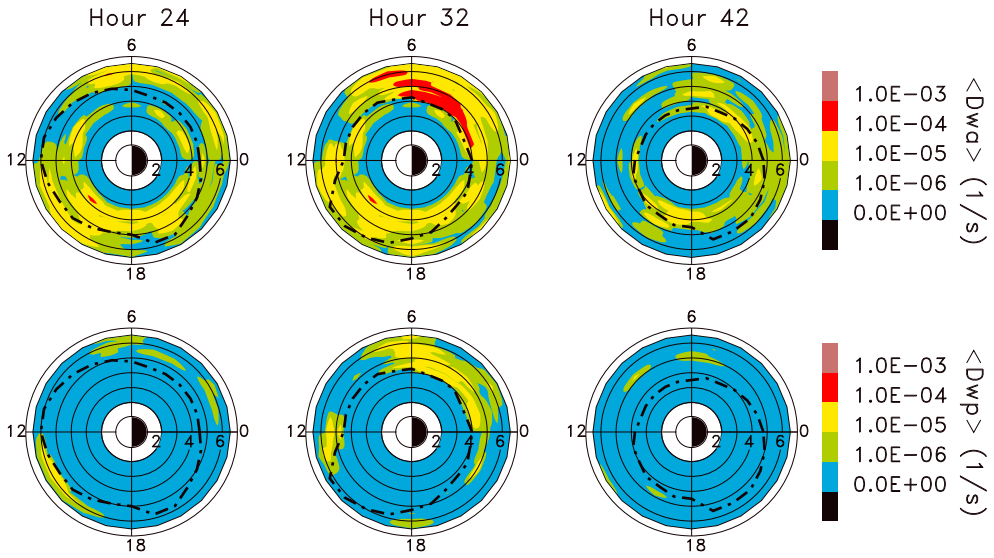

Figure 6. Event-specific (top row) pitch angle $< D_{\alpha_o\alpha_o}/p^2 >$ and (bottom row) momentum $< D_{pp}/p^2 >$ diffusion coefficients calculated for 100 keV electrons and $\alpha_o = 50°$ at hours 24, 32, and 42 after 00 UT 7 October 2012. The plasmapause location is plotted with a dash-dotted line for reference.

In this study the bounce-averaged pitch angle $\langle D_{\alpha_o\alpha_o} \rangle$ and momentum $\langle D_{pp} \rangle$ diffusion coefficients are calculated following the method in *Summers* [2005] assuming field-aligned waves. Global wave intensity distributions in magnetic latitude (MLAT), magnetic local time (MLT), and *L* are required for the calculation. For hiss waves inside the plasmasphere we use the empirical wave distributions statistically derived from the Combined Release and Radiation Effects Satellite (CRRES) wave data, which are binned in *AE** (the mean value of *AE* over the previous 1 h). These wave databases were built at LANL and validated against similar models from *Meredith et al.* [2003, 2004]. The same empirical plasma density models and wave spectral properties were used in *Tu et al.* [2013, Table 1]. However, for whistler mode chorus outside the plasmasphere, which is critical to simulate the strong enhancement of relativistic electrons during the October 2012 storm, we use the global chorus wave proxy of *Chen et al.* [2014] to produce the event-specific chorus wave amplitudes (Figure 5d) as a function of MLT, *L*, and time on a 3 h basis. Since the chorus wave distribution in MLAT cannot be resolved by the proxy, the MLAT dependence from a statistical model is used (also based on CRRES wave data from *Tu et al.* [2013]). Figure 6 shows the equatorial 2-D distribution of the bounce-averaged diffusion coefficients calculated for 100 keV electrons at three representative times. As expected from previous studies, the pitch angle diffusion coefficients are larger than the momentum ones and maximize in the dawn sector during the storm main phase where the chorus wave proxy is most enhanced, corresponding to a minimum electron lifetime of about an hour.

4. Comparison of RAM-SCB Results With Observations

Ring current electron simulations with RAM-SCB during the October 2012 double-dip storm are displayed in Figure 7 where the electron flux was plotted along the Van Allen Probe A trajectory in the same format as in Figure 2 to ease the comparison with MagEIS observations. To this end the spacecraft location was mapped along the 3-D SCB magnetic field lines to the equatorial plane and the RAM flux was obtained by interpolation from neighboring grid points. Figure 7 shows the electron flux averaged over pitch angle obtained with RAM-SCB (version 1) that uses empirical lifetimes for electron loss (middle row), as well as results from the newly developed in this study RAM-SCB (version 2) that includes quasi-linear plasma wave scattering with event-specific diffusion coefficients (bottom row); results from a RAM-SCB test simulation that considers only transport and precipitation losses due to atmospheric collisions at low altitude are shown in the top row for comparison. The modeled fluxes increase during the storm main phase at low energies due to convective transport of newly injected electrons from the plasma sheet in agreement with MagEIS observations (Figure 2), but the model underestimates significantly the fluxes at high (>100 keV) energies in this case. With storm development the flux at lower energies overestimates MagEIS observations when plasma wave scattering losses are not included (Figure 7, top row). On the other hand, the empirical lifetimes used in RAM-SCB

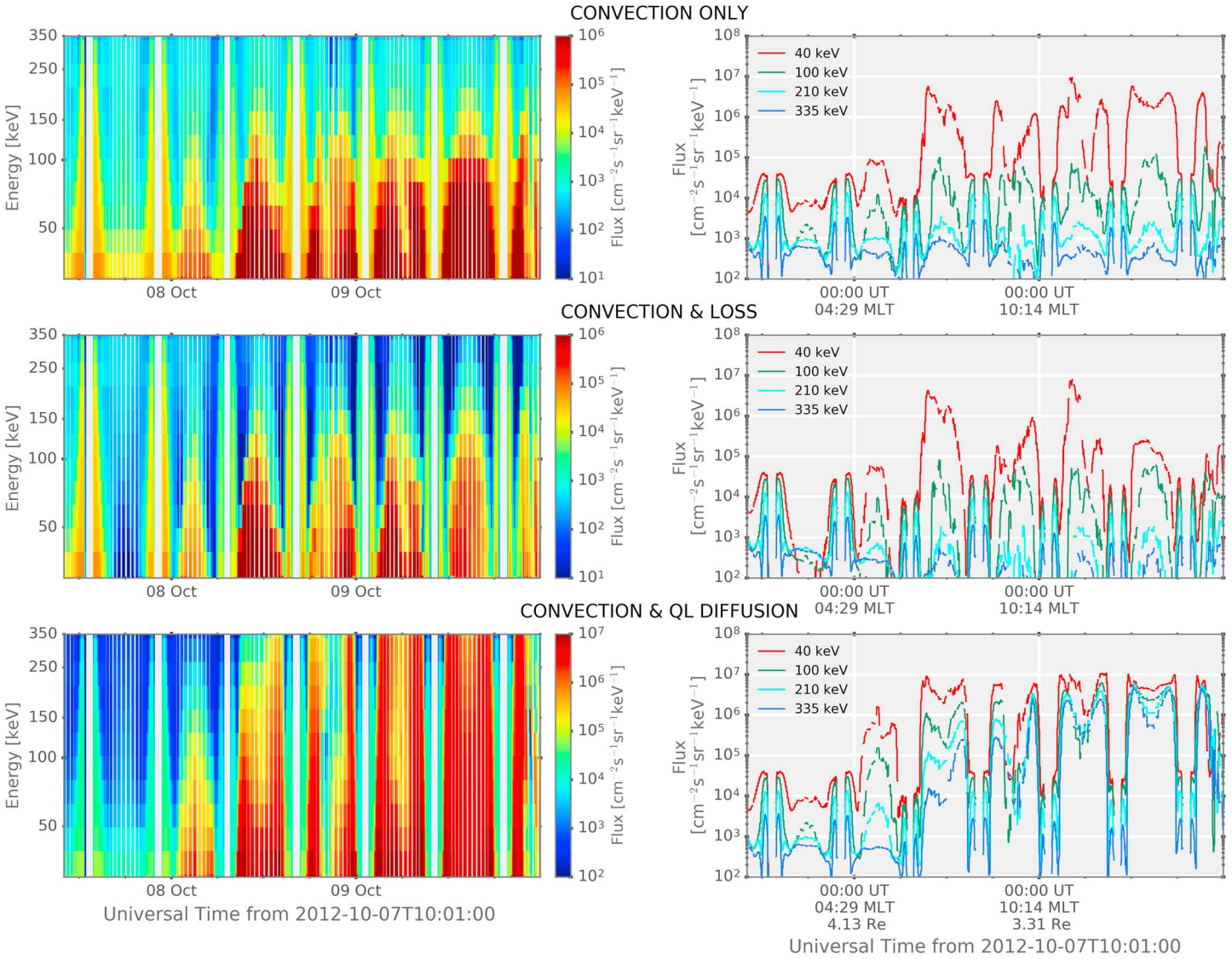

Figure 7. Simulations of electron fluxes averaged over pitch angle and plotted along Van Allen Probe A orbit, (top row) from a RAM-SCB test run considering only transport and loss by atmospheric collisions, (middle row) from RAM-SCB (version 1) using empirical lifetimes for electron loss, and (bottom row) from RAM-SCB (version 2) using quasi-linear diffusion. The vertical white bands indicate successive perigee passes when the satellite is outside the computational domain. The line plots show the electron fluxes at four representative energies: 40 keV (red), 100 keV (green), 210 keV (light blue), and 335 keV (dark blue).

version 1 (Figure 7, middle row) are too short and the electron injection is not large enough to overcome the losses, especially during quiet time and at high energies. Simulations with RAM-SCB version 2 (Figure 7, bottom row) indicate larger fluxes and better agreement with MagEIS data at all energies during quiet time (note the different scales in the plots). As the storm develops the fluxes increase not only at low but also at high energies due to the local acceleration by chorus waves, and while the low-energy flux agrees reasonably well with observations, the flux at $E > 100$ keV becomes about an order of magnitude larger than MagEIS observations near the first *SYM-H* dip. Contrary to observations, the simulated fluxes do not decrease much in the morning sector during the intermediate recovery phase and increase even further during the second *SYM-H* dip significantly overestimating MagEIS fluxes.

In Figure 8 we compare results from several RAM-SCB simulations at $L = 4$ and MLT = 7 with MagEIS data as a function of time. Electron fluxes from the MagEIS spectrometer when the Van Allen Probe A passes through the morning sector at $L \approx 4$ are interpolated onto the RAM energy grid and plotted in Figure 8a. RAM-SCB results considering time-dependent drift and electron loss due to atmospheric collisions at low altitude are shown in Figure 8b, adding pitch angle diffusion by plasma waves in Figure 8c, and adding energy diffusion

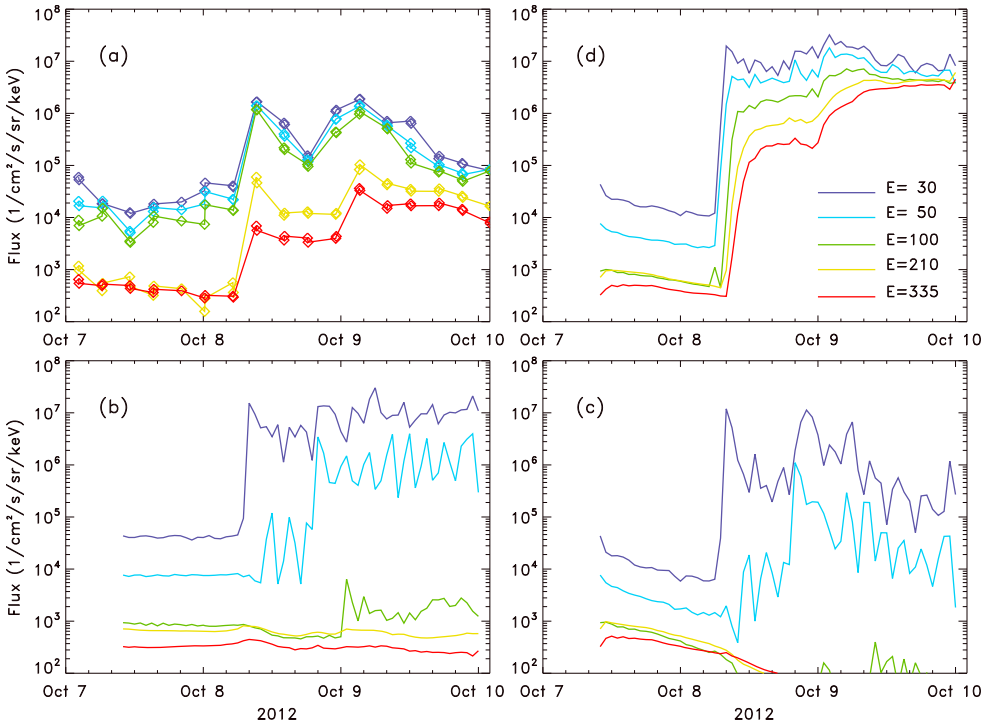

Figure 8. (a) Electron flux measured with MagEIS when the Van Allen Probe A crosses $R_o = 4 \pm 0.1$ R_E during 7–10 October 2012 interpolated onto RAM energy and pitch angle grids. Simulated RAM-SCB electron flux at $L = 4$ and MLT = 7 (b) considering transport and loss due to atmospheric collisions, (c) adding pitch angle scattering, and (d) adding energy scattering, at five representative energies and $\alpha_o = 50°$.

in Figure 8d. In the observations the flux increases at all energies with about 2 orders of magnitude at ~06 UT 8 October during the storm main phase. This is followed by an order of magnitude decrease at ~18 UT during the intermediate recovery phase and a subsequent increase during the second *SYM-H* dip at ~04 UT 9 October to approximately the same magnitude as during the first dip. The first sharp increase is reproduced well by the simulated RAM-SCB flux at 30 keV (Figure 8b). The dynamics of the low-energy electrons is dominated by magnetospheric convection, and the flux rises significantly as the W05 cross polar cap potential drop, indicative of convection strength, and rises at ~06 UT (Figure 1g). With storm development higher-energy electrons penetrate closer to Earth and the 50 keV flux rises at ~10 UT; another rise occurs at ~18 UT. The 100 keV flux rises at ~24 UT, while the increase by convective transport is negligible at higher energies. Note that the small-scale fluctuations clearly seen in the 50 keV flux are representative of "drift echoes," i.e., bunches of injected electrons drifting longitudinally [*Lanzerotti et al.*, 1967], and correspond to the electron drift period of ~3.5 h at this energy. When pitch angle scattering is considered (Figure 8c), the electron flux is reduced, especially at higher energies. The enhancement at these energies is substantial when energy diffusion by plasma waves is included (Figure 8d), and the simulated energy spectra shapes agree better with observations. In this case, however, the fluxes at $E > 50$ keV increase by about 2 orders of magnitude and reach larger values than MagEIS observations during the storm main phase, remain at this elevated level during the intermediate recovery phase, and rise again during the second *SYM-H* dip. Similarly, *Tu et al.* [2014] found that the local heating by chorus during the first *SYM-H* dip overwhelmed the MeV electron loss from outward radial diffusion and the electron distribution did not show a decrease as in the observations but rather an early increase. This indicates that either the local acceleration by chorus waves is overestimated at this time in the event-specific diffusion model or additional loss mechanisms have to be considered.

To provide better understanding of the role various processes have in ring current dynamics, in Figure 9 we plot the electron phase space distribution at $L = 4$ and MLT = 7 during prestorm quiet time at 00 UT 8 October (hour 24) and during the storm main phase at 10 UT 8 October (hour 34). The increasing with geomagnetic storm activity cross-tail electric field moves the boundary between open and closed drift paths inward and allows access of electrons with successively higher energies, from ~20 keV at hour 24 (Figure 9a) to ~80 keV

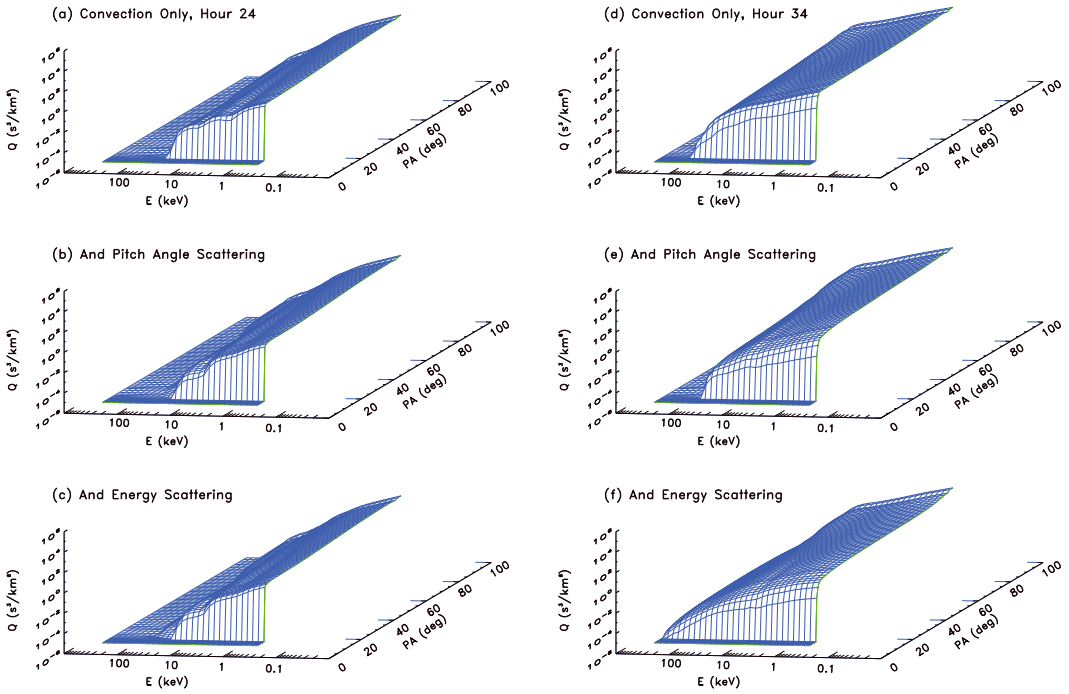

Figure 9. Simulated RAM-SCB electron phase space distribution (s^3/km^6) as a function of energy and pitch angle at $L = 4$ and MLT = 7 (a, d) considering transport and loss due to atmospheric collisions, (b, e) adding pitch angle scattering, and (c, f) adding energy scattering. Figures 9a–9c are at hour 24, while Figures 9d–9f are at hour 34 after 00 UT 7 October 2012.

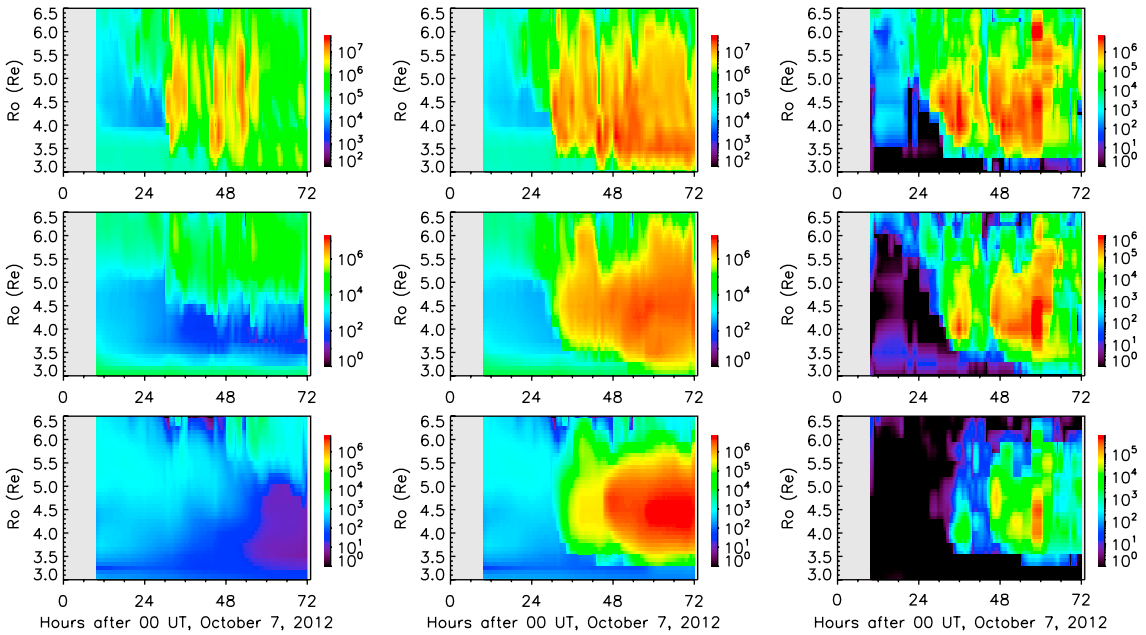

Figure 10. Simulated RAM-SCB flux ($1/cm^2/s/sr/keV$) for 30 keV, 100 keV, and 335 keV (from top to bottom) at MLT = 3 as a function of radial distance from Earth and time after 00 UT 7 October 2012 for trapped electrons ($\alpha_o = 50°$) (left column) considering transport, loss due to atmospheric collisions, and pitch angle scattering and (middle column) adding energy scattering. (right column) Simulated fluxes including all processes for precipitating (mirroring at 200 km altitude) electrons.

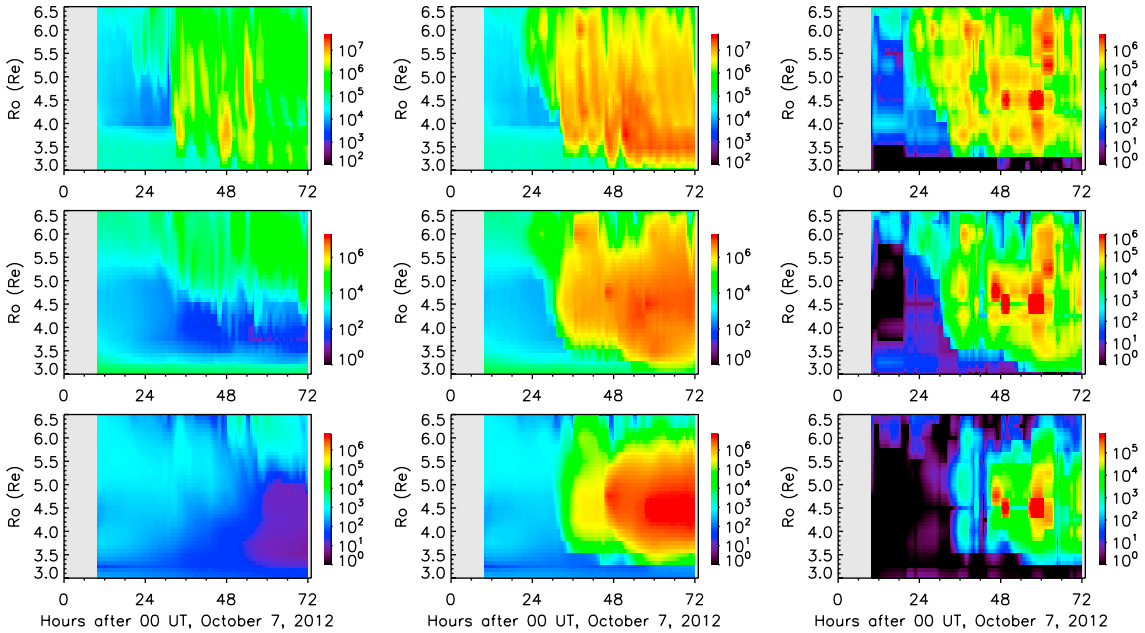

Figure 11. Simulated RAM-SCB electron flux (1/cm^2/s/sr/keV) in the same format as Figure 10 but at MLT = 15.

at hour 34 (Figure 9d). Strong anisotropies thus develop in energy due to the fact that particles with higher energies cannot penetrate the open/closed drift boundary. The process of pitch angle diffusion scatters electrons from larger to smaller pitch angles and reduces the distributions at $E > 5$ keV near the loss cone (Figures 9b and 9e); it does not remove the anisotropy in energy, but it shifts it toward lower energy. Electrons are scattered by energy diffusion from lower to higher energy to reduce this anisotropy (Figures 9c and 9f); this process is more effective at hour 34 due to the stronger wave activity and larger diffusion coefficients. This acceleration effect is more significant than expected because of the large gradients in the distribution function, even though the energy diffusion coefficients are much smaller than the pitch angle diffusion coefficients.

Finally, global patterns of electron fluxes simulated with RAM-SCB are plotted in Figures 10 and 11 in the same L time format as the NOAA POES observations in Figure 3. From top to bottom are shown fluxes at 30 keV, 100 keV, and 335 keV, at MLT = 3 (Figure 10) and MLT = 15 (Figure 11). Fluxes of trapped ($\alpha_o = 50°$) and precipitating (mirroring at 200 km altitude) electrons calculated at every hour are displayed; these correspond roughly to the temporal and spatial resolution and pitch angles sampled by POES detectors. When energy diffusion is not included (left column), the 30 keV electrons penetrate to $L \approx 3$ on the morning side during the storm main phase after convective transport from the plasma sheet and eastward drift, forming an asymmetric ring current in good agreement with POES observations. The electron fluxes at higher energies are very small and considerably underestimate the observations. The fluxes increase due to local acceleration by chorus waves when energy diffusion is included (middle column), the enhancement being larger at higher energies, and the electron distribution becomes symmetric with MLT at $E > 100$ keV as seen in POES observations. During the intermediate recovery phase the trapped high-energy flux decreases at large ($L > 5$) shells but remains enhanced between $L = 4$ and $L = 5$; it increases by an order of magnitude during the second *SYM-H* dip and overestimates POES data. The precipitating flux (right column) follows the temporal and spatial evolution of the trapped flux but is more than an order of magnitude smaller (note the different scales) and reproduces better POES observations.

5. Summary and Conclusions

Mechanisms for particle injection in the near-Earth space environment and their subsequent trapping or loss have been the subject of detailed investigation recently, thanks to the high-resolution data available from the Van Allen Probes. Their theoretical evaluation and numerical implementation in global models with high-fidelity predictive capabilities, however, remains challenging. We studied the combined effects from

time-dependent transport and scattering by whistler mode chorus and hiss on the source (approximately tens of keV) and seed (approximately hundreds of keV) populations of the radiation belts during the October 2012 double-dip storm. We used our kinetic ring current-atmosphere interactions model coupled with a Euler-potential-based three-dimensional plasma equilibrium code (RAM-SCB), including for the first time pitch angle and energy diffusion using L and MLT-dependent event-specific wave models. The chorus wave amplitudes were thus inferred from correlations of POES/MEPED precipitating electron fluxes and RBSP/EMFISIS wave observations; the spatial and temporal evolutions of peak wave amplitudes was in reasonable agreement with chorus growth rate maxima calculated with RAM-SCB. Comparisons of RAM-SCB simulations with complementary data sets from the Van Allen Probes in the morning MLT sector and NOAA POES satellites in the afternoon and predawn sectors indicated the following:

1. During quiet time RAM-SCB electron simulations using L and MLT-dependent event-specific pitch angle and energy diffusion coefficients reproduced much better the in situ satellite observations of ring current electron flux than RAM-SCB simulations using empirical lifetimes, since these lifetimes were too short and overestimated the electron losses.
2. The simulated electron flux at lower ($E < 100$ keV) energies increased during the first and second *SYM-H* dips and decreased during the intermediate recovery phase due to earthward transport in time-dependent convective electric field and nondipolar magnetic field. This electron dynamics was in good agreement with observations of both trapped and precipitating electron fluxes and showed the initial formation of an asymmetric ring current that evolved into a more symmetric one with storm development.
3. At higher ($E \geq 100$ keV) energies RAM-SCB simulations that considered only convective transport and loss substantially underestimated the observations. When local acceleration by chorus was included, the electron fluxes increased by about 2 orders of magnitude during the first *SYM-H* dip, remained enhanced during the intermediate recovery phase at $L = 4$ to $L = 5$, and increased further during the second *SYM-H* dip thus considerably overestimating the satellite observations.

RAM-SCB model results that reproduced significant acceleration by plasma waves at energies as low as ~50 keV were initially unexpected since the energy diffusion coefficients are much smaller than the pitch angle diffusion coefficients. This energization effect is enhanced by the presence of a large energy anisotropy that develops in the electron phase space distribution after particles are injected from the plasma sheet. These results indicate that either additional loss mechanisms (like enhanced losses through the dayside magnetopause or Coulomb collisions) or a better representation of plasma wave scattering taking into account nonlinear effects is needed. A self-consistently calculated electric field, with higher temporal and spatial resolution, will influence both the injection of particles from the tail and their dayside outflow and could result in reduced gradients in the distribution function. Note that the diffusion coefficients themselves depend on many parameters (i.e., wave amplitude, frequency and wave normal distributions, and cold plasma density) which need to be specified with improved temporal and spatial resolution. In addition, other types of plasma waves like magnetosonic and EMIC waves, as well as oblique chorus waves, could produce more scattering and thus influence ring current dynamics. This problem could also be alleviated by including mixed diffusion in RAM-SCB, and this will be considered in future work.

Acknowledgments
Work at Los Alamos was conducted under the auspices of the U.S. Department of Energy, with partial support from the LDRD SHIELDS project, NASA grant NNH14AX90I, Van Allen Probes ECT and EMFISIS funding through JHU/APL contracts 967399 and 921647 under prime NASA contract NAS5-01072, and NSF grant IAA1203460. The work by W. Tu was supported by NSF grant AGS1613081. We thank the OMNIWeb from NASA Goddard Space Flight Center for providing the solar wind observation data and the *AL* and *SYM-H* indices and the NOAA/STP World Data Center for providing the *Kp* index. The Van Allen Probes and NOAA data are available at NASA's CDAWeb data site. The simulation data are available from the corresponding author upon request.

References

Albert, J. M. (1999), Analysis of quasi-linear diffusion coefficients, *J. Geophys. Res.*, *104*, 2429–2441.

Baker, D. N., T. I. Pulkkinen, V. Angelopoulos, W. Baumjohann, and R. L. McPherron (1996), Neutral line model of substorms: Past results and present view, *J. Geophys. Res.*, *101*, 12,975–13,010, doi:10.1029/95JA03753.

Baker, D. N., et al. (2014), Gradual diffusion and punctuated phase space density enhancements of highly relativistic electrons: Van Allen Probes observations, *Geophys. Res. Lett.*, *41*, 1351–1358, doi:10.1002/2013GL058942.

Birn, J., M. F. Thomsen, J. E. Borovsky, G. D. Reeves, D. J. McComas, and R. D. Belian (1997), Characteristic plasma properties during dispersionless substorm injections at geosynchronous orbit, *J. Geophys. Res.*, *102*(A2), 2309–2324, doi:10.1029/96JA02870.

Blake, J. B., et al. (2013), The Magnetic Electron Ion Spectrometer (MagEIS) instruments aboard the Radiation Belt Storm Probes (RBSP) spacecraft, *Space Sci. Rev.*, *179*, 383–421, doi:10.1007/s11214-013-9991-8.

Bortnik, J., and R. M. Thorne (2007), The dual role of ELF/VLF chorus waves in the acceleration and precipitation of radiation belt electrons, *J. Atmos. Sol. Terr. Phys.*, *69*, 378–386, doi:10.1016/j.jastp.2006.05.030.

Chen, M. W., C. L. Lemon, K. Orlova, Y. Shprits, J. Hecht, and R. L. Walterscheid (2015), Comparison of simulated and observed trapped and precipitating electron fluxes during a magnetic storm, *Geophys. Res. Lett.*, *42*, 8302–8311, doi:10.1002/2015GL065737.

Chen, Y., G. Reeves, R. H. W. Friedel, M. F. Thomsen, M. Looper, D. Evans, and J.-A. Sauvaud (2012), LEEM: A new empirical model of radiation-belt electrons in the low-Earth-orbit region, *J. Geophys. Res.*, *117*, A11205, doi:10.1029/2012JA017941.

Chen, Y., G. D. Reeves, R. H. W. Friedel, and G. S. Cunningham (2014), Global time-dependent chorus maps from low-Earth-orbit electron precipitation and Van Allen Probes data, *Geophys. Res. Lett.*, *41*, 755–761, doi:10.1002/2013GL059181.

Elkington, S. R., M. K. Hudson, and A. A. Chan (2003), Resonant acceleration and diffusion of outer zone electrons in an asymmetric geomagnetic field, *J. Geophys. Res.*, *108*(A3), 1116, doi:10.1029/2001JA009202.

Evans, D. S., and M. S. Greer (2000), Polar orbiting environmental satellite space environment monitor: 2. Instrument descriptions and archive data documentation, *NOAA Tech. Memo. OAR SEC-91*, SEC, NOAA, Boulder, Colo.

Fok, M.-C., N. Y. Buzulukova, S.-H. Chen, A. Glocer, T. Nagai, P. Valek, and J. D. Perez (2014), The Comprehensive Inner Magnetosphere-Ionosphere Model, *J. Geophys. Res. Space Physics*, *119*, 7522–7540, doi:10.1002/2014JA020239.

Fu, H. S., J. B. Cao, B. Yang, and H. Y. Lu (2011a), Electron loss and acceleration during storm time: The contribution of wave-particle interaction, radial diffusion, and transport processes, *J. Geophys. Res.*, *116*, A10210, doi:10.1029/2011JA016672.

Fu, H. S., Y. V. Khotyaintsev, M. André, and A. Vaivads (2011b), Fermi and betatron acceleration of suprathermal electrons behind dipolarization fronts, *Geophys. Res. Lett.*, *38*, L16104, doi:10.1029/2011GL048528.

Fu, H. S., Y. V. Khotyaintsev, A. Vaivads, M. André, V. A. Sergeev, S. Y. Huang, E. A. Kronberg, and P. W. Daly (2012), Pitch angle distribution of suprathermal electrons behind dipolarization fronts: A statistical overview, *J. Geophys. Res.*, *117*, A12221, doi:10.1029/2012JA018141.

Funsten, H., et al. (2013), Helium, Oxygen, Proton, and Electron (HOPE) mass spectrometer for the Radiation Belt Storm Probes mission, *Space Sci. Rev.*, *179*, 423–484, doi:10.1007/s11214-013-9968-7.

Horne, R. B., and R. M. Thorne (1998), Potential waves for relativistic electron scattering and stochastic acceleration during magnetic storms, *Geophys. Res. Lett.*, *25*, 3011–3014.

Horne, R. B., R. M. Thorne, S. A. Glauert, N. P. Meredith, D. Pokhotelov, and O. Santolik (2007), Electron acceleration in the Van Allen radiation belts by fast magnetosonic waves, *Geophys. Res. Lett.*, *34*, L17107, doi:10.1029/2007GL030267.

Hudson, M. K., S. R. Elkington, J. G. Lyon, and C. C. Goodrich (2000), Increase in relativistic electron flux in the inner magnetosphere: ULF wave mode structure, *Adv. Space Res.*, *25*, 2327–2337.

Jaynes, A. N., et al. (2015), Source and seed populations for relativistic electrons: Their roles in radiation belt changes, *J. Geophys. Res. Space Physics*, *120*, 7240–7254, doi:10.1002/2015JA021234.

Jordanova, V. K. (2012), The role of the Earth's ring current in radiation belt dynamics, in *Dynamics of the Earth's Radiation Belts and Inner Magnetosphere, Geophys. Monogr. Ser.*, vol. 199, edited by D. Summers et al., pp. 303–313, AGU, Washington, D. C., doi:10.1029/2012GM001330.

Jordanova, V. K., and Y. Miyoshi (2005), Relativistic model of ring current and radiation belt ions and electrons: Initial results, *Geophys. Res. Lett.*, *32*, L14104, doi:10.1029/2005GL023020.

Jordanova, V. K., J. U. Kozyra, A. F. Nagy, and G. V. Khazanov (1997), Kinetic model of the ring current-atmosphere interactions, *J. Geophys. Res.*, *102*, 14,279–14,291.

Jordanova, V. K., C. J. Farrugia, J. M. Quinn, R. M. Thorne, K. E. Ogilvie, R. P. Lepping, G. Lu, A. J. Lazarus, M. F. Thomsen, and R. D. Belian (1998), Effect of wave-particle interactions on ring current evolution for January 10–11, 1997: Initial results, *Geophys. Res. Lett.*, *25*, 2971–2974.

Jordanova, V. K., J. Albert, and Y. Miyoshi (2008), Relativistic electron precipitation by EMIC waves from self-consistent global simulations, *J. Geophys. Res.*, *113*, A00A10, doi:10.1029/2008JA013239.

Jordanova, V. K., R. M. Thorne, W. Li, and Y. Miyoshi (2010a), Excitation of whistler mode chorus from global ring current simulations, *J. Geophys. Res.*, *115*, A00F10, doi:10.1029/2009JA014810.

Jordanova, V. K., S. Zaharia, and D. T. Welling (2010b), Comparative study of ring current development using empirical, dipolar, and self-consistent magnetic field simulations, *J. Geophys. Res.*, *115*, A00J11, doi:10.1029/2010JA015671.

Jordanova, V. K., D. T. Welling, S. G. Zaharia, L. Chen, and R. M. Thorne (2012), Modeling ring current ion and electron dynamics and plasma instabilities during a high-speed stream driven storm, *J. Geophys. Res.*, *117*, A00L08, doi:10.1029/2011JA017433.

Kessel, R. L., N. J. Fox, and M. Weiss (2013), The Radiation Belt Storm Probes (RBSP) and space weather, *Space Sci. Rev.*, *179*, 531–543, doi:10.1007/s11214-012-9953-6.

Kim, H.-J., and A. A. Chan (1997), Fully adiabatic changes in storm time relativistic electron fluxes, *J. Geophys. Res.*, *102*(A10), 22,107–22,116, doi:10.1029/97JA01814.

Kletzing, C. A., et al. (2013), The electric and magnetic field instrument suite and integrated science (EMFISIS) on RBSP, *Space Sci. Rev.*, *179*, 127–181, doi:10.1007/s11214-013-9993-6.

Lanzerotti, L. J., C. S. Roberts, and W. L. Brown (1967), Temporal variations in the electron flux at synchronous altitudes, *J. Geophys. Res.*, *72*(23), 5893–5902, doi:10.1029/JZ072i023p05893.

Li, X., and M. A. Temerin (2001), The electron radiation belt, *Space Sci. Rev.*, *95*, 569–580.

Liu, S., M. W. Chen, J. L. Roeder, L. R. Lyons, M. Schulz, and Geophys. Res. Lett. (2005), Relative contribution of electrons to the stormtime total ring current energy content, *32*, L03110, doi:10.1029/2004GL021672.

Lyons, L. R., R. M. Thorne, and C. F. Kennel (1972), Pitch angle diffusion of radiation belt electrons within the plasmasphere, *J. Geophys. Res.*, *77*(19), 3455–3474.

McIlwain, C. E. (1966), Magnetic coordinates, *Space Sci. Rev.*, *5*, 585–598.

Meredith, N. P., R. B. Horne, R. M. Thorne, and R. R. Anderson (2003), Favored regions for chorus-driven electron acceleration to relativistic energies in the Earth's outer radiation belt, *Geophys. Res. Lett.*, *30*(16), 1871, doi:10.1029/2003GL017698.

Meredith, N. P., R. B. Horne, R. M. Thorne, D. Summers, and R. R. Anderson (2004), Substorm dependence of plasmaspheric hiss, *J. Geophys. Res.*, *109*, A06209, doi:10.1029/2004JA010387.

Meredith, N. P., R. B. Horne, S. A. Glauert, R. M. Thorne, D. Summers, J. M. Albert, and R. R. Anderson (2006), Energetic outer zone electron loss timescales during low geomagnetic activity, *J. Geophys. Res.*, *111*, A05212, doi:10.1029/2005JA011516.

Morley, S. K., R. H. W. Friedel, E. L. Spanswick, G. D. Reeves, J. T. Steinberg, J. Koller, T. Cayton, and E. Noveroske (2010), Dropouts of the outer electron radiation belt in response to solar wind stream interfaces: Global positioning system observations, *Proc. R. Soc. A*, *466*, 3329–3350, doi:10.1098/rspa.2010.0078.

O'Brien, T. P., M. D. Looper, and J. B. Blake (2004), Quantification of relativistic electron microburst losses during the GEM storms, *Geophys. Res. Lett.*, *31*, L04802, doi:10.1029/2003GL018621.

Omura, Y., N. Furuya, and D. Summers (2007), Relativistic turning acceleration of resonant electrons by coherent whistler mode waves in a dipole magnetic field, *J. Geophys. Res.*, *112*, A06236, doi:10.1029/ 2006JA012243.

Paulikas, G. A., and J. B. Blake (1979), Effects of the solar wind on magnetospheric dynamics: Energetic electrons at the synchronous orbit, in *Quantitative Modeling of Magnetospheric Processes, Geophys. Monogr. Ser.*, vol. 21, edited by W. P. Olson, pp. 180–202, AGU, Washington, D. C.

Rasmussen, C. E., S. M. Guiter, and S. G. Thomas (1993), Two-dimensional model of the plasmasphere: Refilling time constants, *Planet. Space Sci.*, *41*, 35.

Reeves, G. D., S. K. Morley, R. H. W. Friedel, M. G. Henderson, T. E. Cayton, G. Cunningham, J. B. Blake, R. A. Christensen, and D. Thomsen (2011), On the relationship between relativistic electron flux and solar wind velocity: Paulikas and Blake revisited, *J. Geophys. Res.*, *116*, A02213, doi:10.1029/2010JA015735.

Reeves, G. D., et al. (2013), Electron acceleration in the heart of the Van Allen radiation belts, *Science*, *341*(6149), 991–994, doi:10.1126/science.1237743.

Rodger, C. J., M. A. Clilverd, J. C. Green, and M. M. Lam (2010), Use of POES SEM-2 observations to examine radiation belt dynamics and energetic electron precipitation into the atmosphere, *J. Geophys. Res.*, *115*, A04202, doi:10.1029/2008JA014023.

Rostoker, G., S. Skone, and D. N. Baker (1998), On the origin of relativistic electrons in the magnetosphere associated with some geomagnetic storms, *Geophys. Res. Lett.*, *25*, 3701–3704.

Schulz, M., and L. J. Lanzerotti (1974), *Particle Diffusion in the Radiation Belts, Phys. and Chem. in Space*, vol. 7, Springer, New York.

Shprits, Y. Y., R. M. Thorne, R. Friedel, G. D. Reeves, J. Fennell, D. N. Baker, and S. G. Kanekal (2006), Outward radial diffusion driven by losses at magnetopause, *J. Geophys. Res.*, *111*, A11214, doi:10.1029/2006JA011657.

Spence, H. E., et al. (2013), Science goals and overview of the Radiation Belt Storm Probes (RBSP) Energetic Particle, Composition, and Thermal Plasma (ECT) suite on NASA's Van Allen Probes mission, *Space Sci. Rev.*, *179*, 311–336, doi:10.1007/s11214-013-0007-5.

Summers, D. (2005), Quasi-linear diffusion coefficients for field-aligned electromagnetic waves with applications to the magnetosphere, *J. Geophys. Res.*, *110*, A08213, doi:10.1029/2005JA011159.

Summers, D., R. M. Thorne, and F. Xiao (1998), Relativistic theory of wave-particle resonant diffusion with application to electron acceleration in the magnetosphere, *J. Geophys. Res.*, *103*, 20,487–20,500.

Thomsen, M. F., M. G. Henderson, and V. K. Jordanova (2013), Statistical properties of the surface-charging environment at geosynchronous orbit, *Space Weather*, *11*, 237–244, doi:10.1002/swe.20049.

Thorne, R. M., and C. F. Kennel (1971), Relativistic electron precipitation during magnetic storm main phase, *J. Geophys. Res.*, *76*, 4446–4453.

Thorne, R. M., et al. (2013), Rapid local acceleration of relativistic radiation-belt electrons by magnetospheric chorus, *Nature*, *504*, 411–414, doi:10.1038/nature12889.

Tu, W., G. S. Cunningham, Y. Chen, M. G. Henderson, E. Camporeale, and G. D. Reeves (2013), Modeling radiation belt electron dynamics during GEM challenge intervals with the DREAM3D diffusion model, *J. Geophys. Res. Space Physics*, *118*, 6197–6211, doi:10.1002/jgra.50560.

Tu, W., G. S. Cunningham, Y. Chen, S. K. Morley, G. D. Reeves, J. B. Blake, D. N. Baker, and H. Spence (2014), Event-specific chorus wave and electron seed population models in DREAM3D using the Van Allen Probes, *Geophys. Res. Lett.*, *41*, 1359–1366, doi:10.1002/2013GL058819.

Walt, M., and W. M. MacDonald (1962), Diffusion of electrons in the Van Allen radiation belt: 1. Treatment of particles with mirroring points at high altitude, *J. Geophys. Res.*, *67*, 5013–5024.

Weimer, D. R. (2005), Improved ionospheric electrodynamic models and application to calculating Joule heating rates, *J. Geophys. Res.*, *110*, A05306, doi:10.1029/2004JA010884.

Wrenn, G. L., D. J. Rodgers, and K. A. Ryden (2002), A solar cycle of spacecraft anomalies due to internal charging, *Ann. Geophys.*, *20*, 953–956.

Zaharia, S., V. K. Jordanova, M. F. Thomsen, and G. D. Reeves (2006), Self-consistent modeling of magnetic fields and plasmas in the inner magnetosphere: Application to a geomagnetic storm, *J. Geophys. Res.*, *111*, A11S14, doi:10.1029/2006JA011619.

Zaharia, S., V. K. Jordanova, D. T. Welling, and G. Toth (2010), Self-consistent inner magnetosphere simulation driven by a global MHD model, *J. Geophys. Res.*, *115*, A12228, doi:10.1029/2010JA015915.